Earth and Planetary Science Letters 296 (2010) 459–468

Contents lists available at ScienceDirect

Earth and Planetary Science Letters

journal homepage: www.elsevier.com/locate/epsl

Imaging a steeply dipping subducting slab in Southern Central America

Laura S. MacKenzie [a], Geoffrey A. Abers [b,*], Stéphane Rondenay [c], Karen M. Fischer [d]

[a] Schlumberger Data and Consulting Services, 6501 S. Fiddler's Green, Greenwood Village, CO 80111, United States
[b] Lamont-Doherty Earth Observatory of Columbia University, 61 Rte 9W, P.O. Box 1000, Palisades NY, 10964, United States
[c] Department of Earth, Atmospheric and Planetary Sciences, Massachusetts Institute of Technology, Cambridge MA 02139, United States
[d] Department of Geological Sciences, Brown University, 324 Brook St., Box 1846, Providence, RI 02912, United States

ARTICLE INFO

Article history:
Received 13 October 2009
Received in revised form 17 May 2010
Accepted 26 May 2010
Available online 26 June 2010

Editor: L. Stixrude

Keywords:
subduction
receiver function migration
Central America
MARGINS
Wadati–Benioff Zones
volcanic arcs

ABSTRACT

Subduction of oceanic lithosphere leads to large changes in seismic velocities that are observable through converted and scattered teleseismic waves. In this study, we use teleseismic data from a dense broadband seismic experiment in Central America to image a slab that dips >60°. Although strongly bent, up going *P*-to-*S* mode conversions show a strong signal from 60–200 km depth; reverberations do not reach the surface because the slab dips steeply here. The subducted oceanic plate is successfully imaged to 200 km depth in Nicaragua where station geometry is adequate, but only at periods near 6 s at depths >100 km, compared with 1–2 s periods for shallower structure. The long-period nature of the deeper conversion indicates a gradational boundary rather than a discontinuity, probably marking the thermal boundary layer at the slab-wedge interface. A sharper discontinuity is imaged near the top of the slab at depths <80 km, probably denoting the Cocos plate Moho. Seismicity lies above the boundary at depths <80 km, and below the inferred thermal boundary at greater depth. The change of character of the discontinuity with depth may reflect partial eclogitization of the subducting crust and associated reduction of the velocity contrast at the Moho, with seismicity lying within subducting crust but the dominant velocity change migrating out of it with increasing depth. In the upper plate, images map the Moho in both Costa Rica and Nicaragua, with Moho conversions weakest directly beneath the arc. Complex dipping structure at 25–50 km depth beneath the Nicaragua forearc perhaps reveals the deep roots of an accreted arc terrane.

1. Introduction

Subduction of oceanic lithosphere at continental margins results in compositional and thermal changes in both the subducted lithosphere and overlying mantle wedge. The sensitivity of seismic velocities to both of these changes allows for characterization of subduction zone processes. Tomographic and receiver function studies take advantage of these velocity changes to image subducting slabs. However, body wave travel time tomography uses volumetric averaging, which precludes identification of sharp boundaries between or within plates. Receiver function studies have the advantage of imaging velocity contrasts associated with compositional and thermal changes within the slab and mantle wedge. Migration of receiver functions has imaged subduction zones in other parts of the world (e.g. Rondenay et al., 2001, 2008; Nicholson et al., 2005), however these studies image slabs with dips <30° to depths of ~100 km. The results presented in this paper show that such migration techniques can be extended to slabs exhibiting dips >60°, with the ability to recover subduction zone structure successfully to 200 km depth.

Several techniques exist to analyze information from scattered waves vary in complexity from simple receiver function stacking (e.g. Ammon, 1991; Langston, 1979) to receiver function migration (e.g. Levander et al., 2005; Pavlis, 2005; Rondenay et al., 2005). Using both direct and reflected phases increases resolution of structure relative to direct-wave-only imaging (Neal and Pavlis, 2001; Poppeliers and Pavlis, 2003). Previous applications of this method have successfully imaged slabs in Alaska (Rondenay et al., 2008), Cascadia (Bostock et al., 2002; Nicholson et al., 2005; Rondenay et al., 2001), and Greece (Suckale et al., 2009), where the slab dips <30° at depths <120 km. These studies all use both direct and surface-reflected phases to resolve subducting oceanic crust as a low velocity layer with thickness ranging from 6–23 km. However, as we show below, the high-resolution phases cannot image more steeply dipping structures.

Here, we test the limits of the two-dimensional migration method (Bostock et al., 2001; Rondenay et al., 2001) by applying it in Central America, where slab dip exceeds 60° at >80 km depth. Such a steep dip is past the theoretical limits of recovery for some converted phases. We analyze the conditions under which steep structures can be imaged and discuss implications for subduction zone dynamics. This complements other recent receiver function studies in Central America. DeShon and Schwartz (2004) stacked receiver functions to estimate crustal thickness and velocity structure for a single GSN

* Corresponding author. Tel.: +1 845 365 8539; fax: +1 845 365 8150.
E-mail addresses: lmackenzie@slb.com (L.S. MacKenzie), abers@ldeo.columbia.edu (G.A. Abers), rondenay@mit.edu (S. Rondenay), Karen_Fischer@brown.edu (K.M. Fischer).

0012-821X/$ – see front matter © 2010 Elsevier B.V. All rights reserved.
doi:10.1016/j.epsl.2010.05.033

station in Costa Rica. MacKenzie et al. (2008) applied a grid search method to stack receiver functions and simultaneously determine crustal structure with *Vp*/*Vs*, at 48 regionally distributed stations (Fig. 1). However, neither method properly images dipping structures, leading to uncertainty in interface location, and neither study imaged the steeply dipping slab expected from seismicity.

2. Data and methods

2.1. Data

As part of the TUCAN (Tomography and other things Under Costa Rica And Nicaragua) experiment, 48 broadband seismic stations were deployed across Nicaragua and Costa Rica from July 2004 through March 2006 (Fig. 1), using a variety of sensors from the IRIS/PASSCAL (Incorporated Research Institutions for Seismology/Program for Array Seismic Studies in Continental Lithosphere) instrument pool. While all stations are used for preprocessing (see Section 2.2), just two dense cross-arc transects with an average station spacing of 10 km are used here for imaging (Fig. 1). We use both *P* and *PP* arrivals from distances between 28° to 90° and 90° to 170°, respectively, from events with body wave magnitude >5.0 and an average event signal-to-noise ratio >3 recorded by more than 10 stations per event.

Several initial quality-control operations are applied to the data set, starting with the rejection of signals that produce unstable deconvolutions (MacKenzie et al., 2008). Next, signals for each individual event are migrated using the technique described in Section 2.3 to determine their separate contribution. Events with obvious spatial aliasing caused by consecutive missing stations or noisy stations are excluded. After the removal of these lower-quality events, the data set consists of 381 records from 34 events, 17 of which use *P* and 17 of which use *PP* as the primary phase (Fig. 1, inset).

All signals are filtered between 0.3 and 0.03 Hz for migration. Higher frequencies are filtered to remove scattering effects from topography at the free-surface (Rondenay, et al., 2005) and lower frequencies are removed to ensure similar frequency content between stations which have corner frequencies of either .033 and .0083 Hz. Somewhat higher frequencies are included in simpler stacks of raw deconvolved signals (Section 4.2).

2.2. Data preprocessing

The scattered wave field is isolated following Bostock and Rondenay (1999), and summarized here. First, the *P* or *PP* wave is isolated in a 90 s window starting just before its onset and transformed to *P*, *SV*, *SH* components using the inverse free-surface transfer matrix (Kennett, 1991), for nominal near-surface velocities. The *P*-wave section is aligned by cross correlation (vanDecar and Crosson, 1990), and the incident and scattered *P* wavefields are separated using principal-component analysis (Ulrych et al., 1999). The incident *P*-wavefield is deconvolved from each of the *SV*, *SH* and scattered *P* components for each station, source-normalizing the scattered *S*-wave and *P*-wave displacement fields. Finally, the wavefield is rotated into a reference frame aligned with slab strike.

2.3. Inversion procedures

The inversion method has been described fully in previous papers (Bostock et al., 2001; Rondenay et al., 2005), and is briefly summarized here. It considers the generation of scattered waves through interaction of an incident teleseismic three-dimensional (3D)

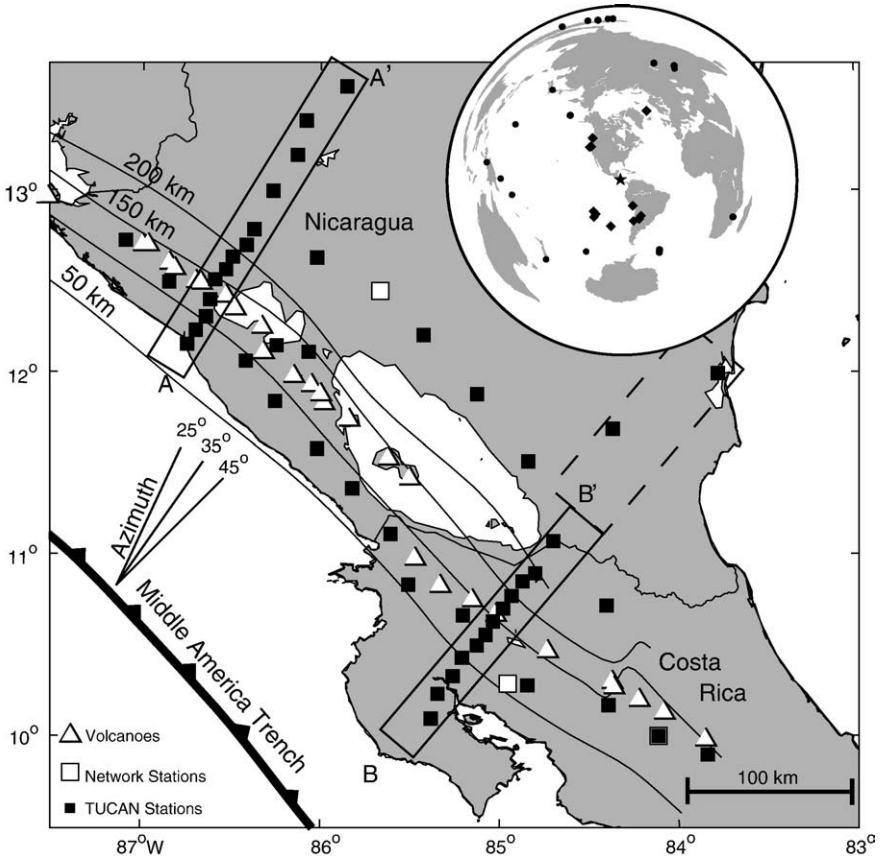

Fig. 1. Station map of region, showing broadband seismographs (squares), volcanoes (triangles), and tectonic features. Labeled contours show depth to intraslab seismicity (Syracuse et al., 2008). Rectangles A–A′ and B–B′ delimit all stations used in the migration, dashed where not shown on images. Inset shows location of region (star) and earthquake sources, utilizing *P* (diamonds) or *PP* (circles).

Table 1
Reference one-dimensional velocity models.

Depth (km)	Costa Rica		Nicaragua		Density (kg/m^3)
	Vp (km/s)	Vs (km/s)	Vp (km/s)	Vs (km/s)	
0–5	5.12	2.92	5.16	2.95	2500
5–10	5.53	2.92	5.52	3.16	2600
10–15	6.03	3.45	5.95	3.41	2600
15–20	6.63	3.78	6.46	3.70	2900
20–25	7.38	4.20	7.09	4.06	3100
25–30	7.50	4.25	7.25	4.13	3100
30–35	7.62	4.30	7.43	4.21	3100
35–40	7.75	4.35	7.62	4.29	3100
40–45	7.89	4.40	7.83	4.38	3500
45–50	7.99	4.50	7.90	4.45	3500
50–300	8.1	4.50	7.98	4.53	3500

wavefield with two-dimensional (2D) lithospheric structure. A back-projection operator, cast as a generalized Radon transform, reconstructs the scattering potential for forward- and back-scattered wavefields. Delay times are calculated in a one-dimensional (1D) reference model, in this case from travel-time tomography (Syracuse et al., 2008), by averaging 3D velocities within the wedge beneath each of the two cross-arc transects A–A′ and B–B′ (Table 1). The inversion solves for material property perturbations (d*Vp*/*Vp* and d*Vs*/*Vs*, where *Vp* and *Vs* denote *P*- and *S*-wave velocities, respectively) for forward scattered *Ps* phases and backscattered or surface-reflected phases (*Ppxp*, *Ppxs*, *Psxs; x* refers to topside reflections off the structure of interest, see Fig. 2). The resulting image shows the velocity variations, d*Vs*/*Vs* or d*Vp*/*Vp*, needed to generate the observed scattered waves. This approach provides benefits relative to inversions for conversion strength (Kirchoff migration); it has been shown in by Bostock (2002) that inversion for conversion strength requires higher frequency signal that is usually contaminated by incoherent and/or unmodelled scattering in teleseismic field-data. Thus the Born-based approach used here, which makes use of lower-frequency signal that can be well extracted from teleseismic wavefields, yields better recovery of subsurface structure. The *P*-wave velocity image shows only weak returns due to signal loss in the preprocessing (Rondenay et al., 2005), and is not discussed further but shown in the Supplementary Data.

3. Resolution

3.1. Sampling

The migration method used here has been applied previously in locations where slab dips are <30°, so direct and reverberated phases could be combined to enhance resolution. Surface-reflected mode conversions improve resolution by roughly a factor of three relative to direct conversions, because of the longer delay times at a given interface depth (Rondenay et al., 2005). Steeper dips pose problems because they cause converted waves to travel over larger lateral offsets (e.g. Cassidy, 1992). Most rays sample the dipping interface at a location updip (trenchward) of the point directly beneath the station, increasingly so with greater dip. Fig. 3 shows the interaction (conversion or top-side reflection) between the slab and the final leg of the scattered wave to the station. In these calculations, rays are traced through dipping layers assuming constant velocities above the interface and a typical ray parameter (0.06 s/km) for the incident *P* wave. In the case of a horizontal interface, the locations of last ray interaction or sampling points from a variety of azimuths form a circle around the station (Fig. 3d). However, layer dip shifts all sampling points updip and compresses the circle in the strike-perpendicular direction (Figs. 3e,f). For example, an interface dipping 30° and located 75 km beneath a station produces a lateral offset of sampling points, 15–20 km trenchward for *Ps* and 40–70 km for *Ppxs* and *Psxs*, relative to their location on a flat-lying interface at the same average depth (Figs. 3b,e). Increasing the dip of the slab offsets these distances further, to the point that recovery within a network spanning only a few hundred kilometers would be impossible (Figs. 3c, f).

A critical dip angle θ_c exists beyond which surface-reflected rays do not reach the surface on their final leg. For a constant-velocity medium and phase *Psxs*, $\cos(2\theta_c) = pV_S$, while for *Ppxs*

$$\tan(\theta_c) = (V_P / V_S - pV_P) / \sqrt{1 - p^2 V_P^2} \quad (1)$$

where p is the ray parameter, and V_P and V_S are the *P* and *S* velocity above the interface, respectively. This critical dip θ_c is 38° for *Psxs* and 56° for *Ppxs*, for the velocities shown on Fig. 3a and a ray parameter of 0.06 (ray propagating downdip). Fig. 3c shows the ray behavior for a slab dipping at only 39°, where the reflected *Psxs* ray does not reach the Earth's surface on its final leg. A more realistic velocity model would curve the ray towards the surface and slightly decrease the ray incidence angle, but the overall effect would be similar: surface-reflected waves *Ppxs* and *Psxs* will not in the end reach the surface for steeply dipping slabs. The Wadati–Benioff zone dips at 60° in central Costa Rica and >70° in Nicaragua at depths >100 km (Protti et al., 1995; Syracuse et al., 2008), so surface-reflected phases reverberating off the top of the slab cannot be observed. This limits us to use only the direct *P*-to-*S* conversion for slab imaging, and requires stations located at suitable lateral offsets from the image points.

Fig. 4 shows the sampling area across the Central America transects for *Ps* waves, indicated at each station by the *Ps* ray path for a vertically incident ray. A vertically incident ray lies in the center of the cone defined by actual rays analyzed, near the center of each ray bundle's sampling area (Fig. 3c). Calculations show that the ray bundle arriving at each station should have a horizontal sampling radius equal to roughly 1/2 the depth of the slab centered on the vertically incident ray. In both Costa Rica and Nicaragua, slabs at depths <100 km are adequately sampled with overlapping sampling areas. As depth exceeds 125 km, sampling becomes less dense, however no large gaps are present in Nicaragua. By contrast, coverage in Costa Rica starts showing large gaps at depths as shallow as ~125 km, since the 2 stations sampling slab at these depths are more than 70 km apart — the paucity of navigable roads in southeast Nicaragua precluded denser station coverage. This limits the overlap of scattered rays and hinders the robustness of the image in Costa Rica.

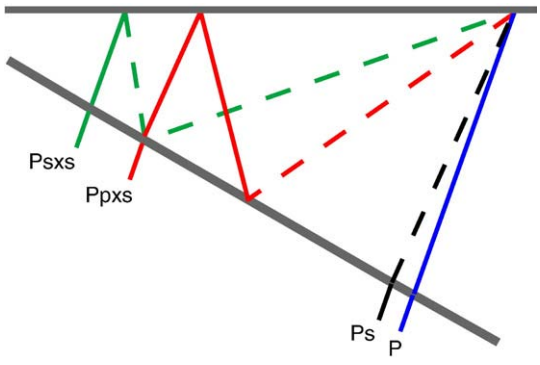

Fig. 2. Ray geometry and phase nomenclature. Solid lines: *P*; dashed: *S*.

3.2. Resolution of thin features

In teleseismic migration, the resolution of layered structure is proportional to the effective scattering wavenumber $f|\nabla T|$, where f is the frequency and ∇T is the spatial gradient of the scattered lag time

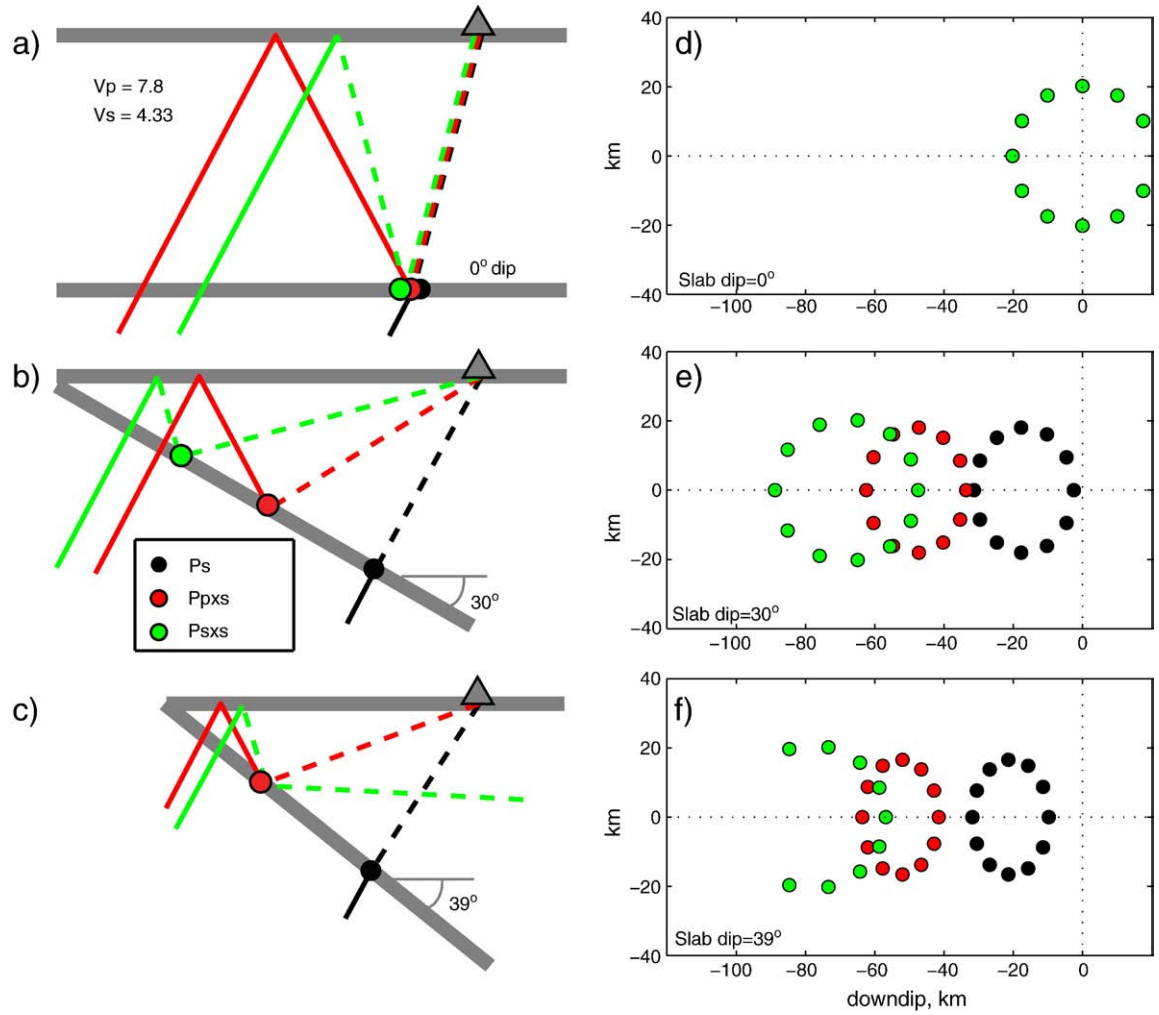

Fig. 3. Ray interactions with dipping interface, for incident P waves with a ray parameter of 0.06 km. a)–c) Reflection/conversion paths for a incident wave coming from updip back azimuths, for interface dips of 0° (a), 30° (b) and 39° (c). Thick lines show interface geometry, triangles show station, thin lines show raypaths solid for *P*, dashed for *S*. Ray segments described as Fig. 2, calculated for $Vp = 7.8$ km/s and $Vs = 4.33$ km/s in the wedge. Note how *Psxs* (green) does not reach surface for slab dips >38°. d)–f) Reflection/conversion points of last ray leg at the dipping interface, in map view, for interface lying 75 km depth directly beneath station, for interface dips of 0° (d), 30° (e) and 39° (f). Axes denote horizontal distances of conversion point from station. Circles colored for phases as denoted by key in b), and plotted only for rays reaching the surface.

(see, e.g., Rondenay, 2009). Here, ∇T is calculated by summing the travel time gradients of the incident wave and the adjoint of the scattered waves intersecting at the image point. The volume resolution, i.e., the minimum spacing necessary to distinguish two neighboring scatterers or discontinuities, is approximately half the signal's wavelength $\lambda/2$ (e.g. Benz and Vidale, 1993; Richards, 1972; Sheriff and Geldart, 1995), such that the resolution limit for our case can be defined as:

$$r_{\min} = \frac{1}{2f_{\max}|\nabla T|} \tag{2}$$

where $r_{\min}$ represents the minimum resolvable structure, and $f_{\max}$ is the maximum frequency in the signal (0.3 Hz).

Applying the scaling of Eq. (2) to image points underneath each networks, we find: (1) for flat layers at continental Moho depths, i.e., ~30 km depth, in the center of both arrays, $r_{\min} = 12$ km for the forward scattering mode and 3–4 km for backscattering modes; (2) for layers with a dip of 50–60° located at 60 km depth beneath the western part of the arrays, $r_{\min} = 11$ km for the forward scattering mode whereas the backscattered modes have zero sensitivity; and (3) for layers with a dip of 60–70° located at 150 km depth beneath the western part of the arrays, $r_{\min} = 9$ km for the forward scattering mode whereas the backscattered modes have zero sensitivity. Given these resolution estimates, we do not expect to resolve the thickness of steeply dipping subducted oceanic crust, which is estimated at 5.5 km (Walther et al., 2000), but we expect nonetheless to detect signal corresponding to this feature.

3.3. Spatial aliasing

Rondenay et al. (2005) have shown that the effects of spatial aliasing due to station spacing only affect the image to a depth equal to twice the station spacing. In both Nicaragua and Costa Rica, spatial aliasing does not affect the Moho in the forearc, owing to the 10 km station spacing there. In the Nicaraguan backarc, 20–25 km station spacing puts the Moho close to the limit of spatial aliasing, while larger station spacing behind the Costa Rica arc may lead to significant spatial aliasing there. As a result, the Costa Rica backarc Moho is unlikely to be imaged well by migration. The stacking approach of MacKenzie et al. (2008), provides crustal thickness estimates directly below the stations, assuming a sub horizontal interface.

4. Results

The highest-resolution images of subhorizontal interfaces such as the Moho include both forward- and back-scattered phases. While forward *P*-to-*S* conversions have the potential to image the slab, the

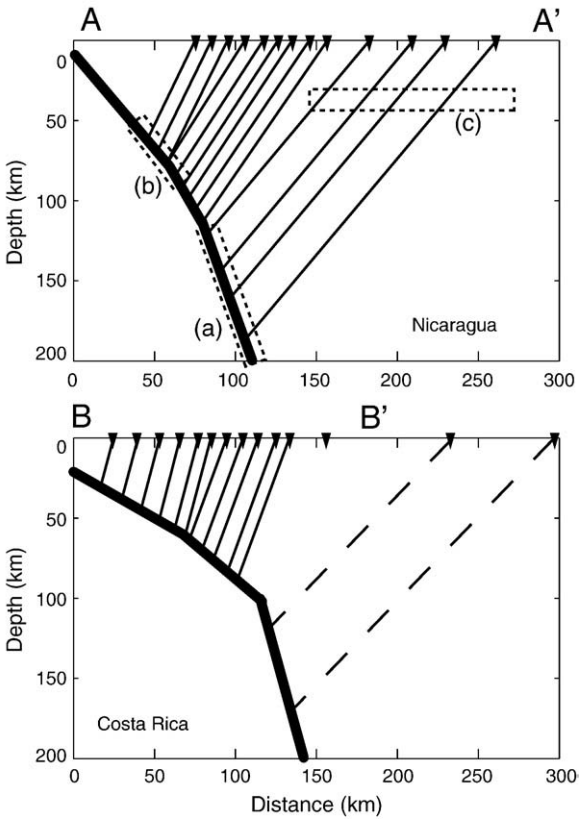

Fig. 4. Region sampled by *Ps* for a dipping slab interface (thick line), accounting for ray bending at *P*-to-*S* conversions on the slab surface. Location of A–A′ (Nicaragua, top) and B–B′ (Costa Rica, bottom) shown on Fig. 1. Thin lines show center of nominal ray bundle sampled by each station, dashed for stations included in migration but not shown in Fig. 6. Dotted boxes show assumed conversion points and ray bundles used in stacks on Fig. 8, corresponding to the letters shown.

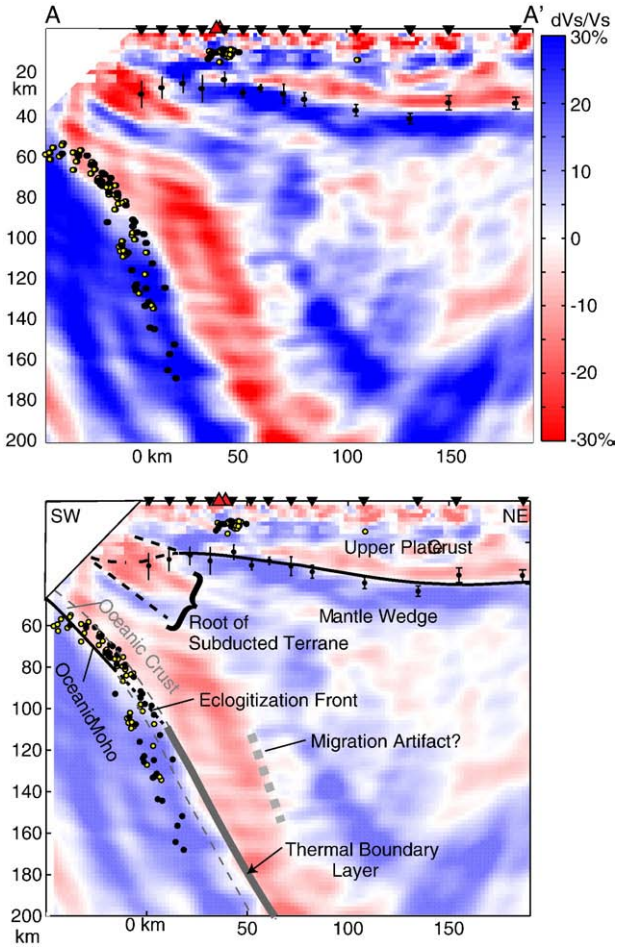

Fig. 5. (Top) Migrated d*Vs*/*Vs* image for the Nicaragua transect A–A′ (location on Fig. 1). Inverted black triangles indicate stations, large upright triangles denote volcanic arc. Small yellow and black dots are relocated earthquakes NW and SE of the station respectively. Black circles with error bars are crustal thickness estimates from MacKenzie et al. (2008). (Bottom) Interpretation of image; color saturation is reduced 50% to make annotations visible.

inclusion of back-scattered conversions that are not sensitive to steeply dipping features adds considerable noise. Thus, standard images produced by combining the contributions of forward- and back-scattering modes (e.g., Rondenay et al., 2001) reveal little subcrustal structure in Central America (see Supplementary Data Fig. S1b). To overcome this limitation, the stacking weight of *Ps* is increased linearly with depth from 25 to 60 km depth, so that the image below 60 km depth is almost completely controlled by the forward-scattered *Ps* mode (Figs. 5, 6).

4.1. Uncertainties

4.1.1. Potential migration artifacts and synthetic image recovery

Several artifacts that appear in the migrated images of Figs. 5 and 6 are common to other applications of the method. First, migration "smiles" resulting from noisy stations, insufficient spatial sampling or internal multiples are observed within the top 10–20 km of both profiles, and at the NE end of the Costa Rica profile. Second, leakage of signal between *Ps*, *Ppxs*, and *Psxs* scattering modes results in occasional multiples in the final image. For example, *Ps* conversions from the Moho can be mapped as *Ppxs* and *Psxs* between 5 and 10 km depth, producing an apparent high velocity discontinuity in this depth range (e.g., Fig. 5). Similarly, the steeply dipping high velocity discontinuity that appears at 100 km depth at the southwest end of the Costa Rican profile (Fig. 6) is most likely a slab multiple. However, the primary structure seen at depths >50 km in Nicaragua, including secondary structure in the mantle, is only found on *Ps* and not from other scattering modes so is not a form of leakage of structure from these modes (see data supplement for individual mode contributions to the image). Signals from other modes do not produce coherent steeply-dipping features, since such interfaces cannot generate *Ppxs* and *Psxs* (Figs. 3, 4).

To test the ability of the migration to recover steep dips from *Ps*, we migrate synthetic seismograms for structure in the same manner as actual data (Fig. 7). In this test, mode conversions are generated from a single dipping interface (Fig. 7a shows velocities and station distribution). Seismograms are calculated from the ray-based algorithm of Frederiksen and Bostock (2000), and processed in the same manner as actual data. Individual mode contributions (Supplementary Fig. S3) confirm that only the *Ps* mode produces conversions, but that *Ppxs* images show faintly a "ghost" of the *Ps* conversion at shallow depths. In the actual inversion (Fig. 5), these ghosts cannot be seen, probably because they are overwhelmed by heterogeneity and near-Moho structure. Two artifacts appear in both these model calculations and the real data, (1) the artificially increased amplitude caused by incomplete sampling in ray angle, and (2) the apparent gradational velocity boundary 50 km into the wedge above the slab interface ("Migration Artifact" in Fig. 5).

The magnitudes of velocity perturbations imaged (Figs. 5, 6) are clearly larger than realistic perturbations expected for such environments. This amplification effect has been documented in synthetic and field data examples (e.g., Rondenay et al., 2005), and can be attributed to the use of sparse data sets in the inversion that causes operator aliasing. Specifically, the aliasing is due to the large station spacing in the NE portion of the profile (~20 km spacing) in conjunction with the

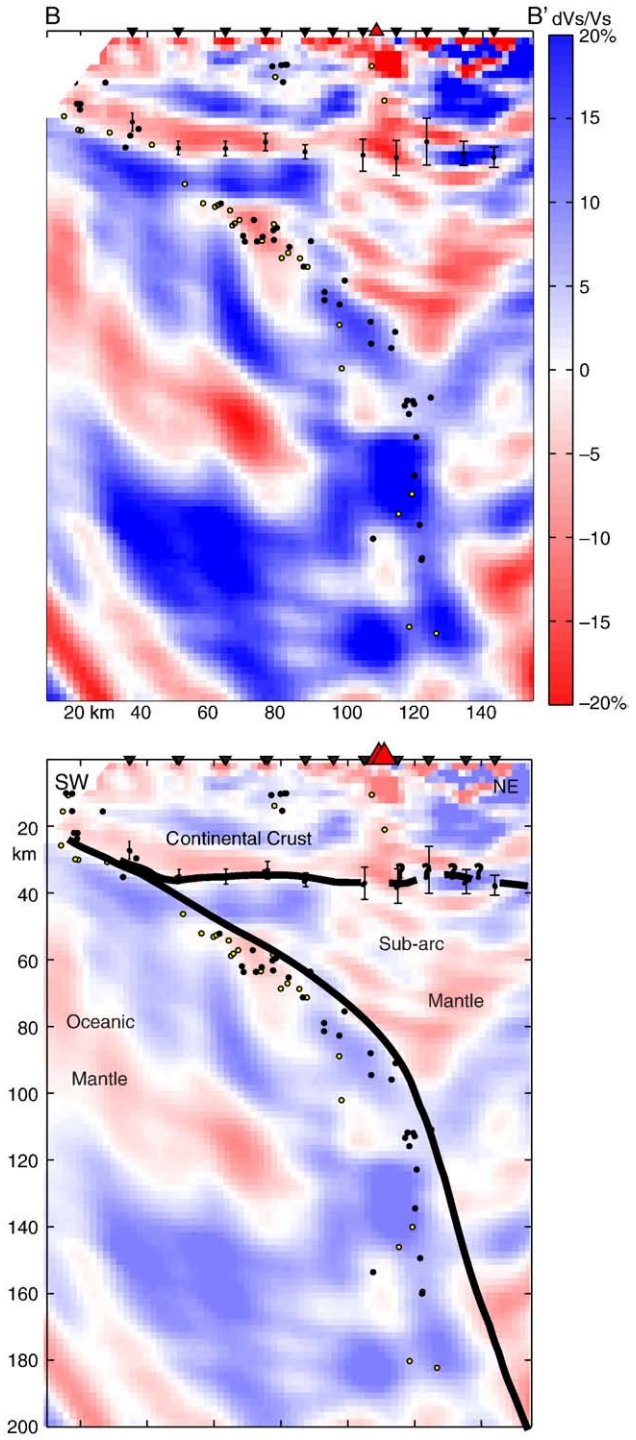

Fig. 6. (Top) Migrated d*Vs*/*Vs* image for the Costa Rica transect B–B′. Format same as Fig. 5. (Bottom) Interpretation of image; color saturation is reduced 50% to make annotations visible.

limited number of events used in the inversion. This effect is reproduced in Fig. 7.

4.1.2. Comparing the image to seismicity

The seismicity shown in Figs. 5 and 6 is relocated in the same background velocity models as those used in the migration. Formal $(1-\sigma)$ uncertainties of earthquake locations range from .02–2.9 km, however formal uncertainties may underestimate true errors since systematic biases are not accounted for (e.g., Pavlis, 1986; Husen et al., 2003a). Additional random errors in relative hypocenters may exist and possible shifts in seismicity relative to the image may result from projection along strike to a single cross section. However, shifts in seismicity relative to the image are reduced as much as possible by relocating earthquakes using the same velocity model used in the migration, at the projection giving the best image (see below).

4.1.3. Orientation and background velocity sensitivity

The migration assumes a 2D structure. The appropriate orientation is presumably the one where dipping structure in the subducted slab is most focused, i.e. the migration produces the sharpest velocity contrast, and seismicity collapses into the tightest line. Multiple projections were tested, at 10 ° increments in azimuth, using these criteria to establish the correct strike (MacKenzie, 2008). For both Nicaragua and Costa Rica, we find that a 45 ° projection azimuth best represents the regional strike.

In order to test the sensitivity of the resulting images and hypocenters to the background velocity model, we reproduced the Nicaragua image using a range of background velocity models in which the *Vp*/*Vs* ratio was varied (MacKenzie, 2008). These variations result in lateral shifts of the slab interface by up to 10 km for *Vp*/*Vs* changes of 0.05. For a given change in background velocity model, we note that hypocenters shift in a similar fashion as the structure, implying that the relationship between seismicity and structure is relatively insensitive to the velocities used. The velocity changes considered here are large, i.e., larger than allowed by the travel time data used to estimate background velocities (Syracuse et al., 2008), so this test represents an upper bound on location uncertainties. In all cases, seismicity crosses the slab discontinuity at a depth of ~85–90 km and lies ~15 km southeast of the slab discontinuity at a depth of 150 km.

Additionally, travel times in the 1D model used for the Nicaragua migration are compared with those calculated for the original 3D model (Syracuse et al., 2008), for paths from a series of slab surface locations to Nicaragua stations. Travel time differences between local 1D and 3D models average <0.1 s for both *P* and *S*. The largest differences (0.4–0.8 s) correspond to near-vertical paths directly beneath the volcanic arc. For most paths controlling the deeper part of the slab (e.g. rays labeled "(a)" in Fig. 4) the differences between the two travel times are 0.15–0.45 s, equivalent to shifts in interfaces of ≤2 km for converted *S* waves. Although this analysis does not take into account all aspects of 3D structure, it indicates that ignoring such structure should result in biases no greater than 2 km. Hypocenters would shift similarly to structure since the relevant ray paths are similar. Finally, static station corrections for hypocenter relocation were estimated but not used, in order to keep the hypocenters and migration image registered to the same velocity model. Their effect on hypocenters was small (a couple km), and if applied in a consistent manner would have comparable effects on the migration image, as many ray paths are similar.

4.2. Nicaragua

The Nicaraguan transect (Fig. 5) shows two robust features. First, the upper-plate Moho is observed as a positive velocity gradient between 26 and 39 km depth across much of the profile. The Moho matches within error the crustal thickness estimates from Mackenzie et al. (2008). Second, the steeply dipping slab is imaged as a velocity increase with depth, in the vicinity of the Wadati–Benioff zone seismicity. At depths <80 km the seismicity lies above this interface, but seismicity lies below this interface at depths >100 km. This interface appears as the bottom of a ~50 km thick dipping low-velocity region above the slab, but the bottom of this low-velocity region (or the top of the subducted slab) has a velocity gradient that is an order of magnitude larger than the top of it. The difference in gradients indicates that the bottom of this low-velocity region may result from a strong velocity step, but the top may be an artifact of the

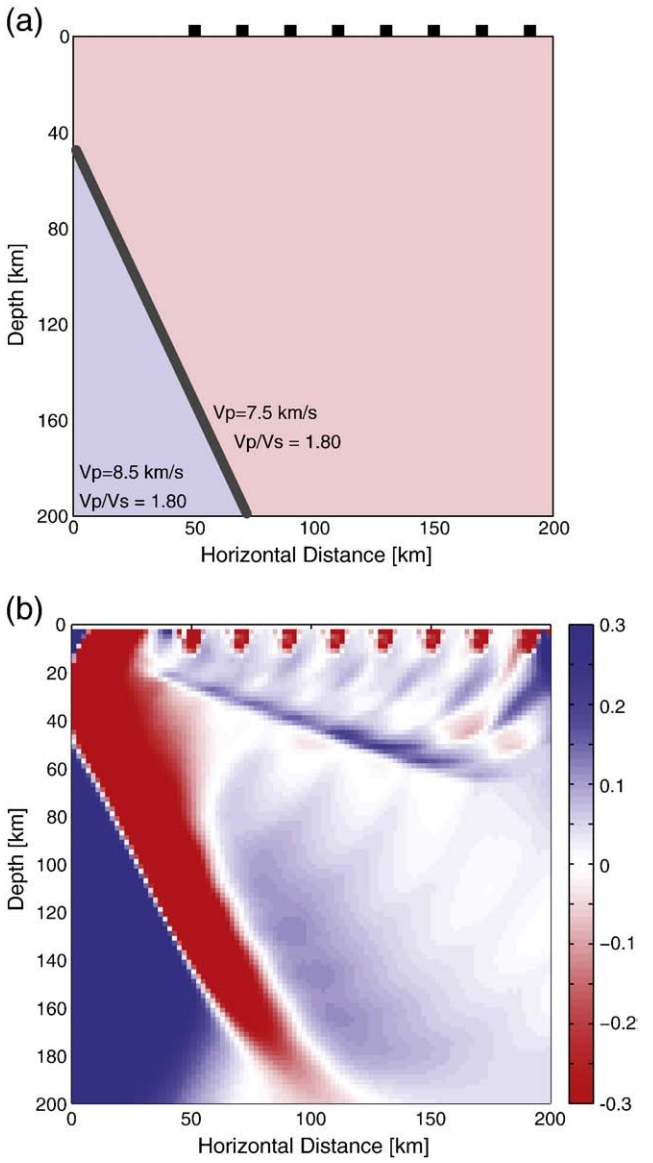

Fig. 7. Migration of synthetic seismograms generated in a model with dipping layers. (a) the model used to generate seismograms; all incident rays come from the left over a range of ray parameters. Black boxes show model stations used, spaced 20 km apart. Seismograms calculated via the algorithm of Frederiksen and Bostock (2000). (b) Processed and migrated seismograms with same parameters as used for actual data. The major, sharp interface is recovered, although amplitude contrasts are ~3× larger than the original model due to incomplete sampling. Other artifacts are discussed in text.

band-limited nature of the signal, as confirmed by synthetic tests (Fig. 7).

To illustrate the nature of the primary interface, individual receiver functions that sample it have been stacked after appropriate alignment (Fig. 8). For the backarc stations that sample the deepest part of the slab, *Ps* raypaths are traced back to a nominal slab surface based on the imaged surface location and dip, and time shifts are calculated for *P*-to-*S* conversions taking into account ray bending. Prior to stacking, the two horizontal component receiver functions are rotated into coordinates perpendicular to strike, since conversions from dipping layers are approximately polarized in this direction and show consistent phase. The receiver functions are realigned by maximizing their cross-correlation prior to stacking in a window around the central peak, with shifts of up to 3 s allow relative to predicted lags, to minimize any pulse broadening caused by heterogeneity-induced phase delays.

The conversion occurring near the inferred surface location (0 s lag on Fig. 8) is pronounced on most records, at least at periods >5 s. The reversed-amplitude conversion indicated by the image at 50 km shallower depth cannot be seen as a coherent signal; it should appear 5–10 s earlier, again confirming that the deeper feature represents a major structure while the shallower one is an artifact.

At shallower depths, the Nicaraguan transect also shows a dipping zone of increased velocity between the continental Moho and the subducting oceanic crust at 25–50 km depth below the SW end of the transect, labeled "Root of Subducted Terrane" on Fig. 5. This zone coincides spatially (within error bars) with a similar feature seen in a coincident active-source wide-angle profile (Walther et al., 2000), a steeply dipping wedge with mantle-like *P*-wave velocities immediately above the subducting oceanic crust, at depths greater than 15 km. The scattered-wave image shows that this structure continues to 40–50 km depth. In the refraction analysis, the feature is interpreted as a remnant of a terrane accreted in the upper Cretaceous (see Section 5.4).

4.3. Costa Rica

The Costa Rican transect (Fig. 6) shows that the upper-plate Moho is a weak but positive (increasing with depth) velocity contrast at ~35 km depth. The Moho signal is strongest at the forearc at horizontal coordinates of 50 to 100 km (0 corresponds to the station nearest to the trench) and corresponds well with crustal thickness estimates by Mackenzie et al. (2008). Southwest of this, the subducting oceanic mantle is probably imaged. Beneath the arc, the upper plate Moho velocity contrast decreases from 15% to <2%, and in the backarc, a weaker Moho is dominated by noise. A steeply dipping high velocity structure exists in the forearc to ~45 km depth corresponding in location with seismicity, and thus probably marks the subducted oceanic slab Moho. Depths are comparable to those inferred from previous single station receiver function analysis (DeShon and Schwartz, 2004), but the image shows Moho structure more clearly. Below 45 km, a discontinuous interface corresponding roughly with the location of seismicity is detected, clearly showing lower velocities above the seismicity than below it, consistent with travel time tomography (Syracuse et al., 2008; Husen et al., 2003b). Coverage is too poor to robustly characterize this feature at depths >100 km.

5. Discussion

5.1. Imaged boundaries of the subducted slab

The slab surface in Nicaragua shows a single, normally polarized velocity contrast (increasing with depth) roughly following seismicity. (The slab in Costa Rica is not imaged as well at subcrustal depths, so discussion here focuses on the Nicaragua result.) Similarly-generated images from Alaska (Rondenay et al., 2008), Vancouver (Nicholson et al., 2005) and Oregon (Rondenay et al., 2001) show a subducting low velocity layer believed to be the subducting oceanic crust, where the primary positive conversion corresponds to oceanic Moho. The imaged interface in both Nicaragua and Costa Rica may be similarly the oceanic Moho, with the top of subducting crust somehow absent. Alternatively, the interface may represent the thermal velocity gradient or boundary layer between the cold subducting slab and overlying mantle wedge. Steady state thermal models (Peacock et al., 2005) predict a lateral temperature change on the order of 800–850º over 15–25 km, at 100 km depth. The method of Hacker and Abers (2004) predicts a 6–9% velocity increase from this temperature change in peridotites. Such a steep velocity gradient would be seen as a discontinuity at sufficiently long wavelengths. A third possibility is that the interface represents the base of a serpentinized or fluid rich layer that lies directly above the subducted

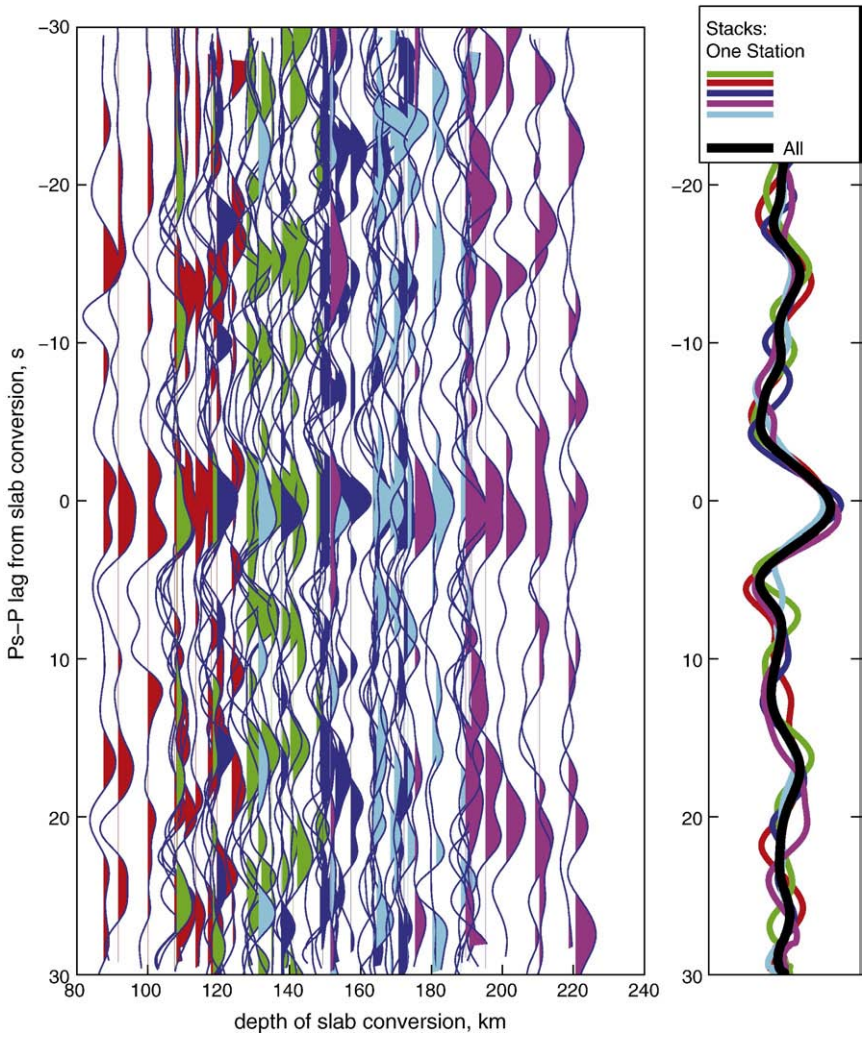

Fig. 8. (Left) Individual receiver functions aligned on expected *P*-to-*S* conversion at slab surface, for the farthest northeast 5 stations on the Nicaragua transect. Rays are traced to a planar dipping surface that follows the highest gradient at 80–200 km depth for all signals used, denoted box (a) on Fig. 4. Traces are aligned such that 0 s lag corresponds to the predicted slab conversion (vertical axis), realigned up to 3 s by cross correlation to account for static offsets, and sorted by lateral position of predicted conversion. All traces show the component polarized downdip to maximize conversions, and are low-pass filtered at 0.13 Hz. (Right) Stacks of receiver functions for each of the 5 stations (colored lines) and entire dataset after cross-correlation (thick black line). A prominent positive conversion can be seen at zero lag, presumably the top of the slab. At −5 s lag the stack shows little coherence, indicating that the subparallel velocity inversion seen in Fig. 5 may be a migration artifact.

oceanic crust (e.g., Iwamori, 2007). Such a layer has been imaged in Japan at depths greater than ~75 km directly above the subducting crust (Kawakatsu and Watada, 2007). However, *Kawakatsu and Watada* image two distinct interfaces in Japan, whereas only a single interface is observed in Nicaragua. It is unclear why such a layer would remain a constant thickness to depths of ~200 km.

To better evaluate these possibilities, we stack the unmigrated Nicaragua receiver functions after correcting them for nominal *Ps* delay times at the observed discontinuity, for the *S* wave component polarized perpendicular to strike (Fig. 8; procedure described in Section 4.2). This stacking is repeated for the slab at 100–200 km depth, 40–70 km depth, and for the backarc continental Moho as a control (Fig. 9). Pulse widths are calculated by fitting Gaussian curves to stacked observations. In this test the original deconvolved records are low-pass filtered at 1 Hz, rather than the 0.3 Hz used for migration, to enhance shorter wavelengths if present. The stacked conversion for both the Moho and shallow slab (Figs. 9b,c) results in a pulse <2 s wide, approximately the minimum resolvable duration given the signal content. These features could be simple discontinuities as often observed for Moho conversions. By comparison, the deeper conversion shows an apparent pulse width of 5.7 s (Fig. 9a), suggesting a wider velocity perturbation. Tests assuming different dips, ranging from 45° to 85°, show that the 65° dip (used in Figs. 8, 9) produces a stack with the largest coherent amplitude and the shortest pulse width, so the broad pulse does not result from incorrect geometry assumptions (see Supplementary Fig. S4). The simplest explanation is that the deeper interface is not a simple discontinuity but rather a gradient zone. The resolution scaling of Eq. (2) indicates a 15–30 km width for such a pulse consistent with the thermal boundary layer.

Given the likely structures present, it seems reasonable that we are imaging the subducting Cocos plate Moho at depths <80 km, and the thermal boundary layer deeper. The 80 km transition depth is similar to that where major dehydration of blueschist minerals may be expected in the crust (Husen et al., 2003b); perhaps the eclogitization of the crust at these depths accounts for the change in character of this interface. The 80 km slab depth also corresponds with the transition from a cold, low-attenuation mantle forearc to hot, high-attenuation sub-arc mantle (Rychert et al., 2008), where a thermal boundary layer should develop at the top of the slab (Abers et al., 2006; Wada et al., 2008). The strong thermal boundary should not exist shallower, while oceanic crust should be eclogitized deeper, producing the observed structure.

At depths >80 km, the top of the subducting oceanic crust is not seen most likely because it has eclogitized. It is less clear why the top

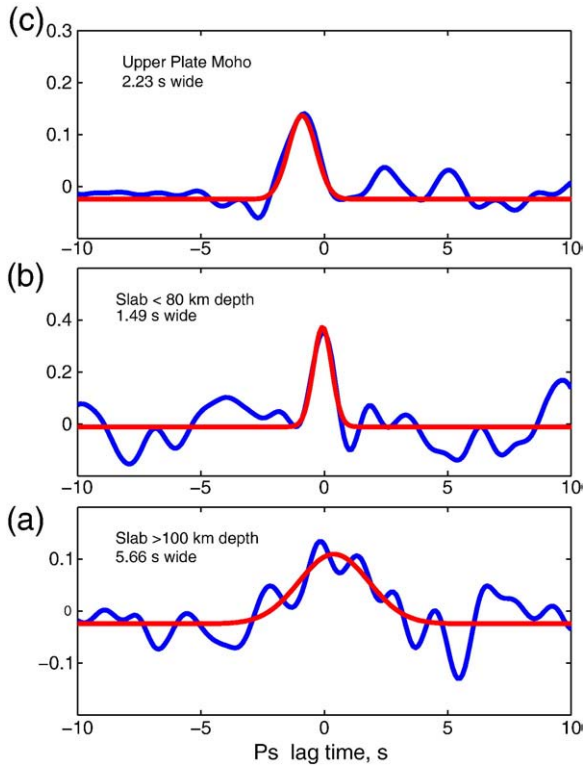

Fig. 9. Stacked *Ps* conversions after aligning on prominent phases (blue lines) and best-fitting Gaussian curve (red lines). (a) Conversions from slab surface 100–200 km deep stacked over 5 northeasternmost stations. (b) Conversions from slab surface 50–80 km deep from 4 stations closest to trench. (c) Conversions from upper plate Moho for 5 northeasternmost stations, to demonstrate changes in pulse width in (a) are not a site artifact. Locations of regions of stacks shown in Fig. 4. All stacks low-pass filtered at 1.0 Hz, different than Fig. 8. Note that (b) and (c) show narrow pulse widths, close to the minimum signal durations allowed by the signal processing, but (a) indicates a much broader mode conversion. Individual traces are cross-correlated prior to stacking to minimize pulse broadening due to velocity variations.

of the subducting crust is not seen at shallower depths, while it is observed elsewhere (e.g., Rondenay et al., 2008). In Nicaragua the slab is sampled at depths only >50 km where dips are steep (Fig. 5), so *Ps* conversions control the image and limit resolution to layers thicker than ~10 km (see Section 3.3). Otherwise, it is possible that the velocity contrast between subducted crust and overlying material is too small. In Cascadia the upper slab interface produces unusually strong mode conversions, requiring low velocities just below the plate interface within the thrust zone, perhaps due to overpressured fluids or thick layers of metasediments (Audet et al., 2009; Abers et al., 2009). These conditions that may be absent in the imaged part of the Central America slab.

5.2. Seismicity

Intermediate-depth seismicity is generally attributed to dehydration embrittlement from breakdown of hydrous minerals within the subducting lithosphere (e.g. Green and Houston, 1995; Hacker et al., 2003; Kirby et al., 1996). In Central America, hydrous minerals are predicted to remain stable in the subducting crust to depths of ~105–120 km before transitioning to eclogite, with hydrous minerals stable in the subducting mantle up to 250 km depth (Hacker et al., 2003; Husen et al., 2003b; Peacock et al., 2005; Rüpke et al., 2002). It appears that seismicity lies within the crust and above the Moho at shallower depths, and below the thermal boundary (perhaps in the crust, perhaps in the mantle) deeper.

5.3. Upper plate crust

The upper-plate crust in Nicaragua is thinnest directly beneath the arc at ~26 km, and is at its thickest point beneath the backarc at ~40 km (Fig. 5). Crustal thickness estimates from Mackenzie et al. (2008) show excellent agreement (error bars on Figs. 5, 6), with minor differences attributable to velocity model differences. The Moho is relatively weak directly beneath the arc and immediate forearc. The presence of either melt in the upper mantle or mafic cumulates at the base of the crust could effectively reduce the velocity contrast between crust and upper mantle. Whereas the crust appears thinnest in Nicaragua directly beneath the arc, the sub-arc crust in Costa Rica appears to be slightly thicker than its surroundings, presumably reflecting interactions with pre-existing structure associated with the Nicaragua Depression (MacKenzie et al., 2008).

5.4. Relict plate

Walther et al. (2000) observe from seismic wide-angle measurements a high-velocity dipping structure overlying the subducting crust in Nicaragua, similar to the slightly deeper feature observed in the forearc wedge here (Fig. 5). They interpret this high velocity sliver as a relict fragment of the Farallon plate mantle that accreted in the late Cretaceous, when an oceanic plateau collided with Central America. More recent studies confirm the presence of mafic–ultramafic Mesozoic basement along the Pacific coast, of primitive arc affinity (e.g., Geldmacher et al., 2008). Thus, the complicated structure imaged here may show the downdip limit of an accreted terrane. It seems reasonable that such features exist undetected beneath many forearcs, as terrane accretion occurs frequently in the geologic record. In these situations, tectonically emplaced crust may partly account for low forearc velocities sometimes attributable to serpentinization (Hyndman and Peacock, 2003). This structure does not extend past the volcanic arc, however, perhaps because flow in the modern mantle wedge has removed any lingering, exotic material. Thus, the terrane roots may be limited to the cold forearc.

6. Concluding remarks

The application of a modified 2D migration method to teleseismic scattered waves recorded by the TUCAN array provides images of continuous structures beneath Costa Rica and Nicaragua, successfully recovering a steeply dipping subducted oceanic slab in Nicaragua. Comparison of the recovery of velocity perturbations between Nicaragua and Costa Rica, with differing array geometries, highlights the necessity of denser station spacing well into the backarc when attempting to image steeply dipping slabs. The subducting crust is imaged as a velocity contrast most likely resulting from the oceanic Moho at shallow depths, transitioning to a gradational velocity contrast at depths >100 km, probably the thermal boundary layer atop this slab. The frequency content of the *Ps* conversion differs between these two depth ranges, in a manner that supports this interpretation. At depths <80 km the Wadati–Benioff zone seismicity lies immediately above the presumed subducting oceanic Moho, while at >100 km depth it lies below the presumed thermal boundary layer, consistent with seismicity located entirely within oceanic crust or perhaps transitioning to the subducting mantle at greater depths. The crustal structure of the overriding plate is well resolved, revealing a crustal thickness of ~35 km in Costa Rica, and a crust ranging from ~26–40 km thick in Nicaragua, with the thinnest crust directly beneath the arc, although Moho is weak to absent directly beneath the arc. Finally, the forearc beneath Nicaragua shows complex structure at 25–50 km depth dipping subparallel to the slab, likely the deep roots of an accreted terrane.

Acknowledgements

We thank E. Syracuse for useful comments and early results from her inversions and thermal models, J.M. Protti, V. Gonzalez, P. Perez, W. Strauch and numerous others for contributions to the TUCAN data collection, and the IRIS/PASSCAL Instrument Pool for technical and logistical support. Comments from two anonymous reviewers significantly improved the manuscript. This work supported by the MARGINS program of the National Science Foundation, grant OCE-0203650.

Appendix A. Supplementary Data

Supplementary data associated with this article can be found, in the online version, at doi:10.1016/j.epsl.2010.05.033.

References

Abers, G.A., van Keken, P.E., Kneller, E.A., Ferris, A., Stachnik, J.C., 2006. The thermal structure of subduction zones constrained by seismic imaging: implications for slab dehydration and wedge flow. Earth Planet. Sci. Lett. 241, 387–397.

Abers, G.A., MacKenzie, L.S., Rondenay, S., Zhang, Z., Wech, A.G., Creager, K.C., 2009. Imaging the source region of Cascadia tremor and intermediate-depth earthquakes. Geology 37, 1119–1122.

Ammon, C.J., 1991. The isolation of receiver effects from teleseismic P-wave-forms. Bull. Seismol. Soc. Am. 81, 2504–2510.

Audet, P., Bostock, M.G., Christensen, N.I., Peacock, S.M., 2009. Seismic evidence for overpressured subducted oceanic crust and sealing of the megathrust. Nature 457, 76–78.

Benz, H.M., Vidale, J.E., 1993. Sharpness of upper-mantle discontinuities determined from high-frequency reflections. Nature 365, 147–150.

Bostock, M.G., 2002. Kirchoff-approximate inversion of teleseismic wavefields. Geophys. J. Int. 149, 787–795.

Bostock, M.G., Rondenay, S., 1999. Migration of scattered teleseismic body waves. Geophys. J. Int. 137, 732–746.

Bostock, M.G., Rondenay, S., Shragge, J., 2001. Multiparameter two-dimensional inversion of scattered teleseismic body waves; 1, Theory for oblique incidence. J. Geophys. Res. 106, 30,771–30,782.

Bostock, M.G., Hyndman, R.D., Rondenay, S., Peacock, S.M., 2002. An inverted continental moho and serpentinization of the forearc mantle. Nature 417, 536–538.

Cassidy, J., 1992. Numerical experiments in broadband receiver function analysis. Bull. Seismol. Soc. Am. 82, 1453–1474.

DeShon, H.R., Schwartz, S.Y., 2004. Evidence for serpentinization of the forearc mantle wedge along the Nicoya Peninsula, Costa Rica. Geophys. Res. Lett. 31, L21611.

Frederiksen, A.W., Bostock, M.G., 2000. Modelling teleseismic waves in dipping anisotropic structures. Geophys. J. Int. 141, 401–412.

Geldmacher, J., Hoernle, K., Van den Bogaard, P., Hauff, F., Klugel, A., 2008. Age and geochemistry of the Central American forearc basement (DSDP Leg 67 and 84): insights into Mesozoic arc volcanism and seamount accretion on the fringe of the Caribbean LIP. J. Petrol. 49, 1781–1815.

Green, H.W., Houston, H., 1995. The mechanics of deep earthquakes. Ann. Rev. Earth Planet. Sci. 23, 169–213.

Hacker, B., Abers, G.A., 2004. Subduction factory 3. An excel worksheet and macro for calculating densities, seismic wave speeds, and H_2O contents of minerals and rocks at pressure and temperature. Geochem. Geophys. Geosyst. 5, Q01005.

Hacker, B., Peacock, S.M., Abers, G.A., Holloway, S.D., 2003. Subduction factory 2. Are intermediate-depth earthquakes in subducting slabs linked to metamorphic dehydration reactions? J. Geophys. Res. 108 art. no. 2030.

Husen, S., Kissling, E., Diechmann, N., Weimer, S., Giardini, D., Baer, M., 2003a. Probabilistic earthquake location in complex three-dimensional velocity models: application to Switzerland. J. Geophys. Res. 108 art. no. 2077.

Husen, S., Quintero, R., Kissling, E., Hacker, B., 2003b. Subduction-zone structure and magmatic processes beneath Costa Rica constrained by local earthquake tomography and petrological modelling. Geophys. J. Int. 155, 11–32.

Hyndman, R.D., Peacock, S.M., 2003. Serpentinization of the forearc mantle. Earth Planet. Sci. Lett. 212, 417–432.

Iwamori, H., 2007. Transportation of H2O beneath the Japan arcs and its implications for global water circulation. Chem. Geol. 239, 182–198.

Kawakatsu, H., Watada, S., 2007. Seismic evidence for deep-water transportation in the mantle. Science 316, 1468–1471.

Kennett, B.L.N., 1991. The removal of free-surface interactions from 3-component seismograms. Geophys. J. Int. 104, 153–163.

Kirby, S., Engdahl, E.R., Denlinger, R., 1996. Intermediate-Depth Intraslab Earthquakes and Arc Volcanism as Physical Expressions of Crustal and Uppermost Mantle Metamorphism in Subducting Slabs. In: Bedout, G.D., Scholl, D.W., Kirby, S., Platt, J. (Eds.), Subduction from top to bottom. Geophys. Monogr., vol. 96. American Geophysical Union, Washington, pp. 195–214.

Langston, C., 1979. Structure under Mount Rainier, Washington, inferred from teleseismic body waves. J. Geophys. Res. 84, 4749–4762.

Levander, A., Niu, F., Symes, W.W., 2005. Imaging Teleseismic P and S Scattered Waves Using the Kirchoff Integral. In: Levander, A., Nolet, G. (Eds.), Seismic Earth: Array Analysis of Broadband Seismograms. Geophys. Monogr., vol. 157. American Geophysical Union, San Francisco, CA, pp. 149–170.

MacKenzie LS (2008) A Receiver Function Study of the Central America and Cascadia Subduction Zone Systems, PhD Thesis, Dept. Earth Sciences. Boston Univ., 162 p.

MacKenzie, L.S., Abers, G.A., Fischer, K.M., Syracuse, E.M., Protti, J.M., Gonzalez, V., Strauch, W., 2008. Crustal thickness along the Southern Central American volcanic front. Geochem. Geophys. Geosyst. 9 Q08S09.

Neal, S.L., Pavlis, G.L., 2001. Imaging P-to-S conversion with broad-band seismic arrays using multichannel time-domain deconvolution. Geophys. J. Int. 147, 57–67.

Nicholson, T., Bostock, M.G., Cassidy, J.F., 2005. New constraints on subduction zone structure in northern Cascadia. Geophys. J. Int. 161, 849–859.

Pavlis, G.L., 1986. Appraising earthquake hypocenter location errors: a complete, practical approach for single-event locations. Bull. Seismol. Soc. Amer. 76, 1699–1717.

Pavlis, G., 2005. Direct Imaging of the Coda of Teleseismic P Waves. In: Levander, A., Nolet, G. (Eds.), Seismic Earth: Array Analysis of Broadband Seismograms. Geophys. Monogr., vol. 157. American Geophysical Union, San Francisco, CA, pp. 171–186.

Peacock, S.M., van Keken, P.E., Holloway, S.D., Hacker, B.R., Abers, G.A., Fergason, R.L., 2005. Thermal structure of the Costa Rica—Nicaragua subduction zone. Phys. Earth Planet. Inter. 149, 187–200.

Poppeliers, C., Pavlis, G.L., 2003. Three-dimensional, prestack, plane wave migration of teleseismic P-to-S converted phases: 2. Stacking multiple events. J. Geophys. Res. 108 art. no. 2267.

Protti, M., Guendel, F., McNally, K., 1995. Correlation between the Age of the Subducting Cocos Plate and the Geometry of the Wadati-Benioff Zone under Nicaragua and Costa Rica. In: Mann, P. (Ed.), Geologic and Tectonic Development of the Caribbean Plate Boundary in southern Central America, vol. 295. Geol. Soc. Amer, Boulder, pp. 309–326. GSA Special Paper.

Richards, P.G., 1972. Seismic waves reflected from velocity gradient anomalies within the Earth's upper mantle. J. Geophys. 38, 517–527.

Rondenay, S., 2009. Upper mantle imaging with array recording of converted and scattered teleseismic waves. Surv. Geophys. 30, 377–405.

Rondenay, S., Bostock, M.G., Shragge, J., 2001. Multiparameter two-dimensional inversion of scattered teleseismic body waves 3. Application to the Cascadia 1993 data set. J. Geophys. Res. 106, 30,795–30, 807.

Rondenay, S., Bostock, M.G., Fischer, K.M., 2005. Multichannel inversion of scattered teleseismic body waves: practical considerations and applicability. In: Levander, A., Nolet, G. (Eds.), Array Analysis of Broadband Seismograms. Geophys. Monogr., vol. 157. Amer. Geophys. Un, San Francisco, CA, pp. 187–204.

Rondenay, S., Abers, G.A., van Keken, P.E., 2008. Seismic imaging of subduction zone metamorphism. Geology 36, 275–278.

Rüpke, L.H., Morgan, J.P., Hort, M., Connolly, J.A.D., 2002. Are the regional variations in Central American arc lavas due to differing basaltic versus peridotitic slab sources of fluids? Geology 30, 1035–1038.

Rychert, C.A., Fischer, K.M., Abers, G.A., Plank, T., Syracuse, E., Protti, J.M., Gonzalez, V., Strauch, W., 2008. Strong along-arc variations in attenuation in the mantle wedge beneath Costa Rica and Nicaragua. Geochem. Geophys. Geosys. 9 Q10S10.

Sheriff, R.L., Geldart, L.P., 1995. Exploration Seismology. Cambridge University Press, New York. 592 pp.

Suckale, J., Rondenay, S., Sachpazi, M., Charalampakis, M., Hosa, A., Royden, L.H., 2009. High-resolution seismic imaging of the western Hellenic subduction zone using teleseismic scattered waves. Geophys. J. Int. 178, 775–791.

Syracuse, E.M., Abers, G.A., Fischer, K.M., MacKenzie, L.S., Rychert, C., Gonzalez, V., Strauch, W., 2008. Seismic tomography and earthquake locations in the Nicaraguan and Costa Rican upper mantle. Geochem. Geophys. Geosyst. 9 Q07S08.

Ulrych, T.J., Sacchi, M.D., Freire, S.L.M., 1999. Eigenimage Processing of Seismic Sections. In: Kirlin, R.L., Done, W.J. (Eds.), Covariance Analysis of Seismic Signal Processing. Geophys. Dev. Ser., vol. 8. Soc. Expl. Geophys, Tulsa.

vanDecar, J.C., Crosson, R.S., 1990. Determination of teleseismic relative phase arrival times using multi-channel cross-correlation and least-squares. Bull. Seismol. Soc. Am. 80, 150–169.

Wada, I., Wang, K., He, J., Hyndman, R.D., 2008. Weakening of the subduction interface and its effects on surface heat flow, slab dehydration, and mantle wedge serpentinization. J. Geophys. Res. 113, B04402.

Walther, C.H.E., Flueh, E.R., Ranero, C.R., von Huene, R., Strauch, W., 2000. Crustal structure across the Pacific margin of Nicaragua: evidence for ophiolitic basement and a shallow mantle sliver. Geophys. J. Int. 141, 759–777.